Solar-Terrestrial Physics. 2019. Vol. 5. Iss. 4. P. 81–90. DOI: 10.12737/stp-54201911. © 2019 O.I. Akhmetov, I.V. Mingalev, O.V. Mingalev, Z.V. Suvorova, V.B. Belakhovsky, S.M. Chernyakov. Published by INFRA-M Academic Publishing House
Original Russian version: O.I. Akhmetov, I.V. Mingalev, O.V. Mingalev, Z.V. Suvorova, V.B. Belakhovsky, S.M. Chernyakov, published in Solnechno-zemnaya fizika. 2019. Vol. 5. Iss. 4. P. 99–109. *DOI: 10.12737/szf-54201911. © 2019 INFRA-M Academic Publishing House (Nauchno-Izdatelskii Tsentr INFRA-M)*

DETERMINATION OF ELF WAVE CHARACTERISTICS MOST STRONGLY REACTING TO MINOR CHANGES OF IONOSPHERIC ELECTRON DENSITY IN A HIGH-LATITUDE REGION

O.I. Akhmetov
Polar Geophysical Institute RAS, Apatity, Russia, akhmetov@pgia.ru

I.V. Mingalev
Polar Geophysical Institute RAS, Apatity, Russia, mingalev_i@pgia.ru

O.V. Mingalev
Polar Geophysical Institute RAS, Apatity, Russia, mingalev_o@pgia.ru

Z.V. Suvorova
Polar Geophysical Institute RAS, Apatity, Russia, suvorova@pgia.ru

V.B. Belakhovsky
Polar Geophysical Institute RAS, Apatity, Russia, belakhovsky@pgia.ru

S.M. Chernyakov
Polar Geophysical Institute RAS, Murmansk, Russia, smcherniakov@gmail.com

Abstract. In this paper, we use numerical experiment methods to address the problem of determining characteristics of ELF (0.3–3 kHz) electromagnetic waves recorded in the surface layer and providing the maximum amount of information about the Earth–ionosphere waveguide. We have analyzed the effect of the horizontal spatial structure of electron density of the Earth–ionosphere waveguide on propagation of electromagnetic waves. We have identified characteristics that allow us to record them by instrumental methods in conditions of weakly disturbed ionosphere. The density profiles used in numerical experiments have been obtained from data acquired by the Partial Reflection Radar at the Polar Geophysical Institute, located at the radiophysical observatory Tumanny in the Murmansk Region (69.0° N, 35.7° E), and by the IRI2016 model during the March 15, 2013 solar flare and the subsequent magnetic storm on March 17, 2013. The electromagnetic signal propagation model used in this work is the adaptation of gas-hydrodynamic methods to electrodynamic applications. The model is based on the scheme of upwind approximation of spatial derivatives (Godunov's method with correction of streams). We also use splitting by spatial directions and physical processes. Signal field attenuation due to conductivity and its rotation due to Hall conductivity of the medium are considered in separate splitting steps by analytical formulas.

Keywords: ELF wave propagation, numerical simulation, ionosphere.

INTRODUCTION

Some of the main problems of radio physics regarding electromagnetic signal propagation in Earth's atmosphere are to search for methods capable of ensuring stable communications or radar (RAdio Detection And Ranging) at different frequencies; to determine conditions when the communication is not possible; to predict the possibility of elimination of such conditions, and to find factors hindering communications or radar. Diagnostics of the ionospheric D-region is important for many physical applications. Currently, the main tried and tested means of such diagnostics are partial reflection radars. Ionosondes and incoherent scatter radars formally cover the D-region, but have a lower accuracy than partial reflection radars [Akimov, Kalinin, 2017]. The ionospheric D layer affects characteristics of electromagnetic signals in ELF (0.3–3 kHz) and VLF (3–30 kHz) ranges. The question, however, remains as to how we can gain the maximum amount of information about D-layer conditions from ground-based measurements of electromagnetic signals in the given range.

In this paper, we use numerical simulation to examine the effect of small (3–5 %) changes in electron density in the D layer on electromagnetic signal characteristics at a frequency of 1500 Hz. We have selected the small changes in electron density to determine the performance potential of D-layer diagnostics by ELF signals. These changes were shown to have no effect on the amplitude of individual components of signal electromagnetic field on Earth's surface, have little effect on the ratio of amplitudes of electric and magnetic field strengths, and marked effect on the phase difference between electric and magnetic field strengths. We have also studied the effect of horizontal dimensions of the region with increased density on the above signal characteristics.

For the numerical simulation of ELF signal propagation, we have used our previously developed model of electromagnetic signal propagation in the atmosphere–lithosphere–ionosphere system. The model numerically integrates the system of Maxwell equations over time on a regular spatial grid. It is based on the explicit scheme of splitting by spatial directions and physical processes with the upstream approximation of spatial derivatives (Godunov's method with correction of streams). This scheme is conservative, monotonic, has a second-order accuracy in time and a third-order accuracy in space.

In the presented numerical experiments, we use a rectangular simulation area and the Cartesian coordinate system, ignoring the curvature of spherical layers of the

lithosphere, atmosphere, and ionosphere for the following reasons. The largest of the horizontal dimensions of the simulation area is about six times less than the Earth radius, whereas the wavelength (~200 km) is comparable with the dimensions of the simulation area. With such a ratio of scales, a signal propagates horizontally without multiple reflections from the ionosphere and lithosphere. The purpose of the simulation is to study the effect of local electron density irregularities in the D-region on electromagnetic signal characteristics. The plane geometry of the simulation area for all the presented numerical experiments gives the same small error, which has no effect on the discussed regularities in the signal characteristics.

SETTING OF THE PROBLEM AND MEDIUM

In this paper, we examine the effect of a slight increase in the electron density in the lower ionosphere at high latitudes on ELF electromagnetic wave propagation at various configurations of horizontal electron density profiles. Medium parameters were set as follows: the neutral particle density was set by the empirical model NRLMSISE-00; electron density and temperature, by the empirical model IRI 2016 with the correction by records from a medium-wave vertical sounding radar designed to explore the lower ionosphere, which is located at the radiophysical observatory Tumanny of the Polar Geophysical Institute in the Murmansk region (69.0° N, 35.7° E) [Tereshchenko et al., 2003], during and after the March 15, 2013 solar flare, namely, on March 15, 2013 at 09:00 UT (disturbed conditions, flare), on March 16, 2013 at 09:00 UT (quiet conditions), on March 17, 2013 at 06:00 UT (disturbed conditions, magnetic storm), and on March 16, 2013 at 06:00 UT (quiet conditions). Vertical electron density profiles under these conditions are shown in Figure 1. The correction involved transferring the fine structure of the D- and E-regions derived from radar data to the profiles obtained with the empirical models IRI 2016 and NRLMSISE.

The March 17, 2013 magnetic storm was triggered by the March 15, 2013 M-class solar flare and began when an interplanetary shock wave, which manifested itself on Earth's surface as SSC (sudden storm commencement) at 06:00 UT, arrived at the magnetosphere.

At this instant, the solar wind velocity increased sharply from ~ 400 to ~650–700 km/s, the IMF B_z component became negative, thus providing a constant energy input to the magnetosphere. The *SYM-H* index characterizing the magnetic storm intensity fell to –100 nT and remained at this level. The auroral *AE* index increased sharply to ~1000 nT and remained increased. At 16:00 UT, *AE* showed the appearance of another auroral activation (an increase in *AE* to ~2500 nT).

At this instant, the solar wind velocity increased sharply from ~ 400 to ~650–700 km/s, the IMF B_z component became negative, thus providing a constant energy input to the magnetosphere. The *SYM-H* index characterizing the magnetic storm intensity fell to –100 nT and remained at this level. The auroral *AE* index increased sharply to ~1000 nT and remained increased. At 16:00 UT, *AE* showed the appearance of another auroral activation (an increase in *AE* to ~2500 nT).

At this instant, the solar wind velocity increased sharply from ~ 400 to ~650–700 km/s, the IMF B_z component became negative, thus providing a constant energy input to the magnetosphere. The *SYM-H* index characterizing the magnetic storm intensity fell to –100 nT and remained at this level. The auroral *AE* index increased sharply to ~1000 nT and remained increased. At 16:00 UT, *AE* showed the appearance of another auroral activation (an increase in *AE* to ~2500 nT).

The horizontal spatial electron density structure can also have an effect on results. To determine this effect, we have carried out three series of experiments with horizontal electron density profiles of different types. The first series simulates the transition from the quiet region to the region with increased electron density. The horizontal electron density profile is shown in Figure 2, *a*. The second series simulates the transition from the region of increased electron density to the quiet region (profile in Figure 2, *b*). The third series simulates the passage through the increased electron density region (Figure 2, *c*). In all the series, the transition was made using the Gaussian function. In the first two series, the horizontal gradient was changed to estimate its effect in the transition region on electromagnetic wave propagation; in the third one, the bandwidth was changed from 0.25λ to λ, where λ is the wavelength. The magnetic field was set vertical, which is typical for high latitudes; its induction was $5.3 \cdot 10^{-5}$ nT.

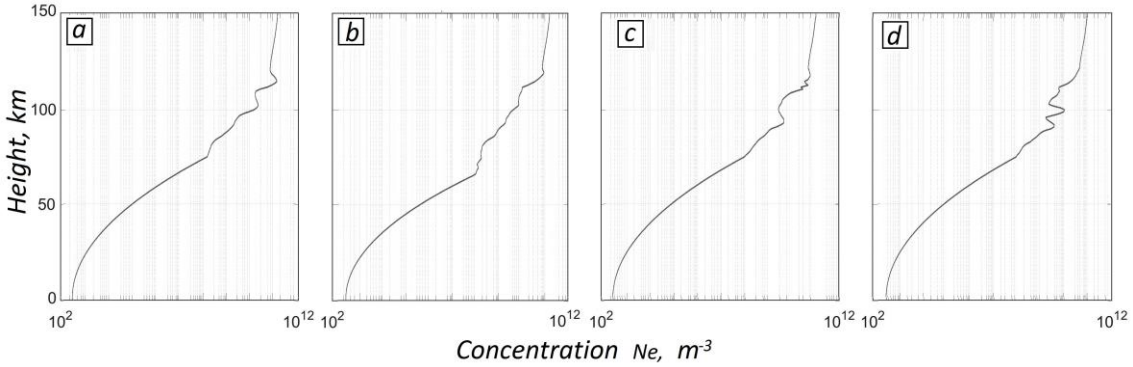

Figure 1. Approximated vertical electron density profiles on March 15, 2013 at 09:00 UT (*a*); on March 16, 2013 at 09:00 UT (*b*); on March 17, 2013 at 06:00 UT (*c*), and on March 16, 2013 at 06:00 UT (*d*)

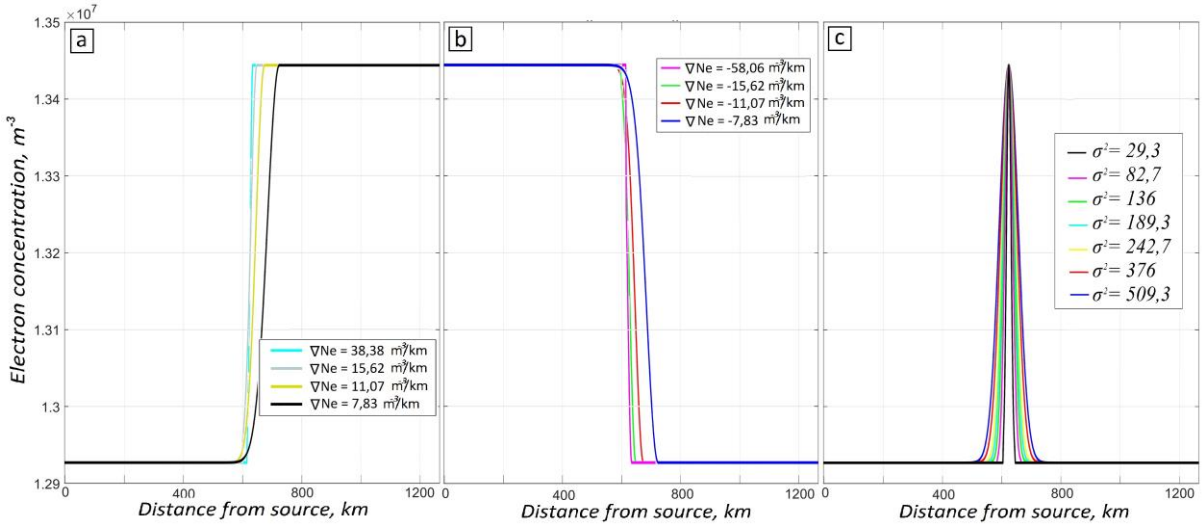

Figure 2. Horizontal electron density profiles for the experiment on electromagnetic wave propagation from the quiet region to the disturbed one (*a*); from the disturbed region to the quiet one (*b*); through the region with increased electron density (*c*)

SIMULATION AREA, SPATIAL GRID, AND SIGNAL SOURCE

In all our numerical experiments, the simulation area was a parallelepiped with a base of 512×1280 km, a height of 150 km in the atmosphere, and a depth of 50 km in the lithosphere. Horizontal grid steps were 2 km; vertical ones, 2 km in the atmosphere and 0.5 km in the lithosphere. The time integration step was $4\cdot10^{-6}$ s.

On all boundaries of the simulation area, we employed special free wave conditions to minimize the influence of unphysical reflections on simulation results. For the simulation, we used a stable harmonic source of signal and analyzed the results when all the processes associated with the passage of a primary signal front (the 35th period of oscillations) stopped. Therefore, despite the almost 100 % signal reflection from the high-conductivity lithosphere and ionosphere inside the simulation area, we employed the same conditions as on horizontal faces of the computational area to avoid accumulation of errors on vertical faces.

As a signal source in all the presented experiments we use a surface of one of the faces of the computational area. This signal source allows us to set not only the amplitude of the signal in time, but also its distribution in space; delays may be used to form the wavefront of the desired shape just as in a plane equidistant phased antenna array [Voskresenskii et al., 2012]. The experiments discussed in this paper simulated a 1500 Hz plane wave (a wavelength of ~200 km) emitted to the area at the right angle to the plane of the source.

DESCRIPTION OF THE MODEL

The model of electromagnetic signal propagation in the Earth–ionosphere waveguide in view of electron inertia in the ionosphere adopted in this paper has been developed through the numerical integration of Maxwell equations over time on a regular spatial grid, using an explicit scheme. It is based on splitting by spatial directions and physical processes. In the scheme, propagation steps for each direction and steps of attenuation and rotation of the electric field alternate. In propagation steps in spatial directions, we also use the upstream approximation of spatial derivatives (Godunov's method with correction of streams). The scheme is conservative, monotonic, has a second-order accuracy in time and a third-order accuracy in space.

Scheme of numerical integration of Maxwell equations in the lithosphere

Let $\mathbf{r}=(x, y, z)$ be the Cartesian coordinates; t be the time; $\mathbf{E}(\mathbf{r}, t)$, $\mathbf{D}(\mathbf{r}, t)$, $\mathbf{H}(\mathbf{r}, t)$, and $\mathbf{B}(\mathbf{r}, t)$ be the magnetic and electric field strength and induction; $\mathbf{j}(\mathbf{r}, t)$ be the current density at t at a point with the radius vector $\mathbf{r}$. Consider the Faraday and Maxwell equations in the SI system

$$\frac{\partial \mathbf{B}}{\partial t} = -\mathrm{rot}\mathbf{E}(\mathbf{r}, t),\ \frac{\partial \mathbf{D}}{\partial t} = \mathrm{rot}\mathbf{H}(\mathbf{r}, t) - \mathbf{j}(\mathbf{r}, t). \quad (1)$$

In the lithosphere, these equations are closed by the Ohm law as

$$\mathbf{j}(\mathbf{r}, t) = \sigma(\mathbf{r})\mathbf{E}(\mathbf{r}, t), \quad (2)$$

where $\sigma(\mathbf{r})$ is the scalar conductivity of the medium, and by constitutive equations

$$\mathbf{D}(\mathbf{r}, t) = \varepsilon_0\varepsilon(\mathbf{r})\mathbf{E}(\mathbf{r}, t),\ \mathbf{B}(\mathbf{r}, t) = \mu_0\mu(\mathbf{r})\mathbf{H}(\mathbf{r}, t), \quad (3)$$

where $\varepsilon(\mathbf{r})$ and $\mu(\mathbf{r})$ are dimensionless relative permittivity and permeability of the medium at a low-frequency limit; ε_0 and μ_0 are electric and magnetic permeability of vacuum.

In the calculations, we assume that in the lithosphere $\mu(\mathbf{r})=1$, but we use μ in subsequent formulas as well because the method in hand allows us to consider the general case with the variable $\mu(\mathbf{r})$.

Let $c_0 = 1/\sqrt{\varepsilon_0\mu_0}$ be the velocity of light in vacuum; $c(\mathbf{r}) = c_0/\sqrt{\varepsilon(\mathbf{r})\mu(\mathbf{r})}$ be the velocity of light in medium at a point with the radius vector $\mathbf{r}$. System (1)–(3) can be written as

$$\frac{\partial \mathbf{B}}{\partial t} = -\mathrm{rot}\mathbf{E},\ \frac{\partial \mathbf{E}}{\partial t} = \frac{c_0^2}{\varepsilon}\mathrm{rot}\left(\frac{\mathbf{B}}{\mu}\right) - \frac{\sigma}{\varepsilon_0\varepsilon}\mathbf{E}. \quad (4)$$

For the numerical integration of (4) we employ the method of splitting by physical processes. The total integration step breaks down into two substeps. One of them is a substep of propagation, at which the system of equations

$$\frac{\partial \mathbf{B}}{\partial t} = -\mathrm{rot}\mathbf{E}, \quad \frac{\partial \mathbf{E}}{\partial t} = \frac{c_0^2}{\varepsilon}\mathrm{rot}\left(\frac{\mathbf{B}}{\mu}\right), \tag{5}$$

is integrated; the second step is a substep of signal attenuation, at which the system of equations

$$\frac{\partial \mathbf{E}}{\partial t} = -\frac{\sigma}{\varepsilon_0 \varepsilon}\mathbf{E}$$

is analytically integrated from formulas $\mathbf{E}(\mathbf{r}, t+\tau) = \mathbf{E}(\mathbf{r}, t)\exp\left(-\frac{\sigma(\mathbf{r})\tau}{\varepsilon_0 \varepsilon(\mathbf{r})}\right)$. The correct sequence of the substeps of splitting provides the second-order accuracy in time.

Consider the numerical integration of (5). Let us introduce renormalized fields $\mathbf{B}(\mathbf{r}, t) = c_0\mathbf{B}(\mathbf{r}, t)$, $\mathbf{E}(\mathbf{r}, t) = c_0 / c(\mathbf{r})\mathbf{E}(\mathbf{r}, t)$, and a vector $\mathbf{M}(\mathbf{r}) = \nabla c$ in the calculations equal to $\mathbf{M}(\mathbf{r}) = \nabla c + c\nabla\mu(\mathbf{r})/\mu(\mathbf{r})$ in the general case. Multiplying the Faraday equation by c_0, we get

$$\frac{\partial \mathbf{B}}{\partial t} = -\mathrm{rot}(c\mathbf{E}). \tag{6}$$

Substituting the introduced notations in the Maxwell equation brings this equation to the form

$$\frac{\partial \mathbf{E}}{\partial t} = \mathrm{rot}\left(c\mathbf{B}\right) - \left[\mathbf{M}\times\mathbf{B}\right]. \tag{7}$$

Let us introduce matrices $\mathbf{R}_x$, $\mathbf{R}_y$, $\mathbf{R}_z$ and zero matrix $\mathbf{O}$:

$$\mathbf{R}_x = \begin{pmatrix} 0 & 0 & 0 \\ 0 & 0 & -1 \\ 0 & 1 & 0 \end{pmatrix}, \mathbf{R}_y = \begin{pmatrix} 0 & 0 & 1 \\ 0 & 0 & 0 \\ -1 & 0 & 0 \end{pmatrix}, \quad \mathbf{R}_z = \begin{pmatrix} 0 & -1 & 0 \\ 1 & 0 & 0 \\ 0 & 0 & 0 \end{pmatrix}, \mathbf{O} = \begin{pmatrix} 0 & 0 & 0 \\ 0 & 0 & 0 \\ 0 & 0 & 0 \end{pmatrix}. \tag{8}$$

The operator rot in Cartesian coordinates can be written as

$$\mathrm{rot}\mathbf{a} = \mathbf{R}_x\frac{\partial \mathbf{a}}{\partial x} + \mathbf{R}_y\frac{\partial \mathbf{a}}{\partial y} + \mathbf{R}_z\frac{\partial \mathbf{a}}{\partial z}. \tag{9}$$

Let us introduce a six-dimensional column-vector of variables $\mathbf{u} = \left(B_x, B_y, B_z, E_x, E_y, E_z\right)^T$ and a vector $\mathbf{F} = \left(F_1, F_2, F_3, F_4, F_5, F_6\right)^T$, whose components are given by

$$F_1 = F_2 = F_3 = 0, \left(F_4, F_5, F_6\right)^T = -\left[\mathbf{M}\times\mathbf{B}\right]. \tag{10}$$

Using notations (8) and Formulas (9) and (10), the system of Equations (6) and (7) can be represented as a vector equation

$$\frac{\partial \mathbf{u}}{\partial t} + \mathbf{A}_x\frac{\partial (c\mathbf{u})}{\partial x} + \mathbf{A}_y\frac{\partial (c\mathbf{u})}{\partial y} + \mathbf{A}_z\frac{\partial (c\mathbf{u})}{\partial z} = \mathbf{F}, \tag{11}$$

where $\mathbf{A}_x$, $\mathbf{A}_y$, $\mathbf{A}_z$ are the 6×6 symmetric matrices given by

$$\mathbf{A}_x = \begin{pmatrix} \mathbf{O} & \mathbf{R}_x \\ -\mathbf{R}_x & \mathbf{O} \end{pmatrix}, \mathbf{A}_y = \begin{pmatrix} \mathbf{O} & \mathbf{R}_y \\ -\mathbf{R}_y & \mathbf{O} \end{pmatrix}, \quad \mathbf{A}_z = \begin{pmatrix} \mathbf{O} & \mathbf{R}_z \\ -\mathbf{R}_z & \mathbf{O} \end{pmatrix}. \tag{12}$$

Vector equation (11) gives a six-dimensional linear hyperbolic system of first-order equations written in the conservative form. Its right part $\mathbf{F}$ depends linearly on components of the vector $\mathbf{u}$. For the numerical integration of such systems many difference schemes have been developed, in particular schemes of higher-order accuracy that are applied to gas dynamics equations. These schemes are described in most detail in monographs [Kulikovskij et al., 2012; Bisikalo et al., 2013].

Using the method of splitting by spatial directions, we can devise clear monotonic schemes of numerical integration of (11), which reduce to successive integration of spatially one-dimensional hyperbolic equations. At each time step, we should successively integrate three systems of equations, for example, in the following order:

$$\frac{\partial \mathbf{u}'}{\partial t} + \mathbf{A}_x\frac{\partial \left(c\mathbf{u}'\right)}{\partial x} = \mathbf{F}_x, \frac{\partial \mathbf{u}''}{\partial t} + \mathbf{A}_y\frac{\partial \left(c\mathbf{u}'\right)}{\partial y} = \mathbf{F}_y, \quad \frac{\partial \mathbf{u}'''}{\partial t} + \mathbf{A}_z\frac{\partial \left(c\mathbf{u}'''\right)}{\partial z} = \mathbf{F}_z. \tag{13}$$

In this case, the right-hand sides of systems (13) are selected so that they remain unchanged in their splitting step and satisfy the equality

$$\mathbf{F} = \mathbf{F}_x + \mathbf{F}_y + \mathbf{F}_z. \tag{14}$$

These conditions are met if we specify them using the formulas

$$\mathbf{F}_x = \left(0, 0, 0, 0, -M_z B_x, M_y B_x\right)^T,$$

$$\mathbf{F}_y \left(0, 0, 0, -M_z B_y, 0, -M_x B_y\right)^T,$$

$$\mathbf{F}_z \left(0, 0, 0, -M_y B_z, M_x B_z, 0\right)^T.$$

At each splitting step for two magnetic field components and two electric field components orthogonal to the step direction, we calculate signal propagation, using a finite-difference method. As initial conditions for each system of equations in (13) we take values calculated in the previous splitting step. We can preserve the second order of the time approximation in the splitting scheme by cyclically changing the order of splitting steps, for example, by first making steps in spatial directions in the following order: *xyz*, *yxz*, *zxy*, *xzy*, *yzx*, *zyx*. This assertion is justified, for example, in [Bisikalo et al., 2013; Kovenja et al., 1981].

Given a uniform grid with respect to $t_n = t_0 + n\tau$,

where τ is the time step, and a uniform spatial grid in Cartesian coordinates whose integer and half-integer nodes are specified by relations

$$x_i = x_0 + ih_x,\ y_j = y_0 + jh_y,\ z_k = z_0 + kh_z,$$
$$r_{i,j,k} = \left(x_i, y_j, z_k\right),$$
$$x_{i+1/2} = x_0 + \left(i+1/2\right)h_x,\ y_{j+1/2} = y_0 + \left(j+1/2\right)h_y,$$
$$z_{k+1/2} = z_0 + \left(k+1/2\right)h_z,$$

where h_x, h_y, h_z are grid steps along the X, Y, and Z axes respectively. For values of the *f* function in the grid nodes we will use notations $f\left(r_{i,j,k}, t_n\right) = f^n_{i,j,k}$.

Consider the layer-by-layer transition for the first system of (13), which is integrated in the splitting step in the direction *x*. In this case, we represent the matrix given by the first formula in (10) $\mathbf{A}_x$ as $\mathbf{A}_x = \mathbf{Q}\mathbf{\Lambda}\mathbf{Q}^{-1}$, where $\mathbf{\Lambda}$ is the diagonal matrix, whose diagonal has eigenvalues of $\mathbf{A}_x$; $\mathbf{Q}$ is the matrix whose columns are right eigenvectors of the matrix $\mathbf{A}_x$, determined up to a factor; $\mathbf{Q}^{-1}$ is the matrix inverse to $\mathbf{Q}$. Rows of the matrix $\mathbf{Q}^{-1}$ are left eigenvectors of $\mathbf{A}_x$. These matrices are constant. They can be taken in the form

$$\mathbf{\Lambda} = \begin{pmatrix} 0 & 0 & 0 & 0 & 0 & 0 \\ 0 & 1 & 0 & 0 & 0 & 0 \\ 0 & 0 & -1 & 0 & 0 & 0 \\ 0 & 0 & 0 & 0 & 0 & 0 \\ 0 & 0 & 0 & 0 & 1 & 0 \\ 0 & 0 & 0 & 0 & 0 & -1 \end{pmatrix},$$

$$\mathbf{Q} = \begin{pmatrix} 1 & 0 & 0 & 0 & 0 & 0 \\ 0 & 1/2 & 0 & 0 & 0 & 1/2 \\ 0 & 0 & 1/2 & 0 & 1/2 & 0 \\ 0 & 0 & 0 & 1 & 0 & 0 \\ 0 & 0 & -1/2 & 0 & 1/2 & 0 \\ 0 & -1/2 & 0 & 0 & 0 & 1/2 \end{pmatrix},$$

$$\mathbf{Q}^{-1} = \begin{pmatrix} 1 & 0 & 0 & 0 & 0 & 0 \\ 0 & 1 & 0 & 0 & 0 & -1 \\ 0 & 0 & 1 & 0 & -1 & 0 \\ 0 & 0 & 0 & 1 & 0 & 0 \\ 0 & 0 & 1 & 0 & 1 & 0 \\ 0 & 1 & 0 & 0 & 0 & 1 \end{pmatrix}.$$

With the matrices $\mathbf{\Lambda}$, $\mathbf{Q}$, and $\mathbf{Q}^{-1}$, we represent the first system of equations in (13) as a vector equation

$$\frac{\partial \mathbf{u}}{\partial t} + \mathbf{Q}\mathbf{\Lambda}\mathbf{Q}^{-1}\frac{\partial (c\mathbf{u})}{\partial x} = \mathbf{F}_x. \qquad (15)$$

We introduce a column vector of characteristic variables (linearized Riemann invariants) in the direction *x*, given by the formula $\mathbf{w} = \mathbf{Q}^{-1}\mathbf{u}$. Components of the vector **w** are given by

$$w_1 B_x,\ w_2 = B_y - E_z,\ w_3 = B_z - E_y,$$
$$w_4 = E_x,\ w_5 = B_z + E_y,\ w_6 = B_y + E_z.$$

Multiply Equation (15) on the left by $\mathbf{Q}^{-1}$. The result is a vector equation

$$\frac{\partial \mathbf{w}}{\partial t} + \mathbf{\Lambda}\frac{\partial (c\mathbf{w})}{\partial x} = \mathbf{Q}^{-1}\mathbf{F}_x, \qquad (16)$$

which is a system of six scalar equations for characteristic variables.

As a result, the numerical integration of the first system of (13) reduces to the numerical integration of four independent spatially one-dimensional transfer equations (16) for characteristic variables

$$w_2 = B_y - E_z,\ w_3 = B_z - E_y,$$
$$w_5 = B_z + E_y,\ w_6 = B_y + E_z.$$

This integration is made using the explicit upwind scheme having the third-order accuracy in space and the second-order accuracy in time. This scheme is described in detail in [Mingalev et al., 2018a, b].

Let us briefly consider the main ideas underpinning the numerical scheme.

Scheme of numerical integration of Maxwell equations in the ionosphere

For the ionosphere, we assume that the dimensionless relative permeability of the medium $\mu(\mathbf{r}) = 1$ and the formula $\mathbf{B}(\mathbf{r}, t) = \mu_0\mathbf{H}(\mathbf{r}, t)$ is fulfilled. We also suppose that there is plasma polarization $\mathbf{D}\left(\mathbf{r}, t\right) = \varepsilon_0\mathbf{E}(\mathbf{r}, t) + \mathbf{P}(\mathbf{r}, t)$, where $\mathbf{P}(\mathbf{r}, t)$ is the polarization vector, the polarization current density $\partial\mathbf{P}/\partial t = \mathbf{j}$ coinciding with the total current density in plasma. The Faraday and Maxwell equations in this case take the form

$$\frac{\partial \mathbf{B}}{\partial t} = -\mathrm{rot}\mathbf{E},\ \frac{\partial \mathbf{E}}{\partial t} = c_0^2\mathrm{rot}\mathbf{B} - \frac{2}{\varepsilon_0}\mathbf{j}. \qquad (17)$$

System (17) is closed by the equation for the density of the electron current generated by the signal field:

$$\frac{\partial \mathbf{j}}{\partial t} = -\nu_e\mathbf{j} - \Omega_e\left[\mathbf{j}\times\mathbf{b}\right] + \omega_e^2\varepsilon_0\mathbf{E},$$

where ν_e is the electron collision frequency, $\Omega_e = e\left|\mathbf{B}_{\text{вн}}\right|/m_e$ is the electron gyrofrequency, $\mathbf{B}_{\text{ext}}$ is the external geomagnetic field, $\mathbf{b} = \mathbf{B}_{\text{вн}}/\left|\mathbf{B}_{\text{вн}}\right|$, $\omega_e^2 = e^2 n_e/\left(m_e\varepsilon_0\right)$ is the squared electron plasma frequency.

In the ionosphere, as in the lithosphere, the method of splitting by physical processes is applied. The correct sequence of the splitting substeps provides the second-order accuracy in time. At the propagation substep, we take into account only signal propagation and numerically integrate the system of equations

$$\frac{\partial \mathbf{B}}{\partial t} = -\mathrm{rot}\mathbf{E},\ \frac{\partial \mathbf{E}}{\partial t} = c_0^2\mathrm{rot}\mathbf{B} \qquad (18)$$

using the same scheme as for System (5) in the lithosphere.

At the signal attenuation and rotation substeps, the signal magnetic field does not change, and only the electron field attenuation and rotation due to the external geomagnetic field are taken into account. At each point of the computational grid, we analytically integrate the system of equations

$$\frac{\partial \mathbf{E}}{\partial t} = -\frac{2}{\varepsilon_0}\mathbf{j},\ \frac{\partial \mathbf{j}}{\partial t} = -\nu_e \mathbf{j} - \Omega_e \left[\mathbf{j}\times\mathbf{b}\right] + \omega_e^2 \varepsilon_0 \mathbf{E}. \qquad (19)$$

This system is divided into two independent systems for field-aligned electric field $E_{\parallel} = (\mathbf{b}, \mathbf{j})$ and current $j_{\parallel} = (\mathbf{b}, \mathbf{j})$

$$\frac{\partial E_{\parallel}}{\partial t} = -\frac{2}{\varepsilon_0} j_{\parallel},\ \frac{\partial j_{\parallel}}{\partial t} = -\nu_e j_{\parallel} + \omega_e^2 \varepsilon_0 E_{\parallel} \qquad (20)$$

and transverse electric field $\mathbf{E}_{\perp} = \mathbf{E} - \mathbf{b}E_{\parallel}$ and current $\mathbf{j}_{\perp} = \mathbf{j} - \mathbf{b}\, j_{\parallel}$:

$$\begin{aligned} &\frac{\partial \mathbf{E}_{\perp}}{\partial t} = -\frac{2}{\varepsilon_0}\mathbf{j}_{\perp}, \\ &\frac{\partial \mathbf{j}_{\perp}}{\partial t} = -\nu_e \mathbf{j}_{\perp} - \Omega_e \left[\mathbf{j}_{\perp}\times\mathbf{b}\right] + \omega_e^2 e_0 \mathbf{E}_{\perp}. \end{aligned} \qquad (21)$$

Systems (20) and (21) are self-contained linear systems of homogeneous differential equations (HDE) with constant coefficients. Solutions of the Cauchy problem for these systems are expressed by rather cumbersome analytical formulas.

In this part of the ionosphere, where the inequality $\nu_e \tau \geq 20$, holds, systems (20) and (21) are replaced by simpler equations and system

$$\begin{aligned} &\frac{\partial E_{\parallel}}{\partial t} = -\frac{2\omega_e^2}{\nu_e} E_{\parallel}, \\ &\frac{\partial \mathbf{E}_{\perp}}{\partial t} = -\frac{2\omega_e^2 \nu_e}{\nu_e^2 + \Omega_e^2}\left(\mathbf{E}_{\perp} - \frac{\Omega_e}{\nu_e}\left[\mathbf{E}_{\perp}\times\mathbf{b}\right]\right), \end{aligned}$$

which also have analytical solutions of the Cauchy problem.

The above scheme allows us to consider the frequency dispersion and simulate propagation of broadband signals of arbitrary form.

Conditions on the boundary of the simulation area

In the model experiments, on all external boundaries we set a free wave boundary condition, which was achieved by zeroing the stream incoming from outside the simulation area. This approach provides low coefficients of reflection of a plane wave from the simulation area boundaries: for waves incident at an angle of 80° to 90°, the ratio of the amplitude of the reflected wave to the amplitude of the incident plane wave does not exceed 0.01. At an incidence angle of 60°, this ratio is already ~0.05; at an angle of 45°, ~0.16; at an angle of 27°, ~0.33; and at an angle of 18.4°, ~0.43 [Mingalev et al., 2018a]. By comparison: the FDTD method (finite-differences time-domain method) [Yee, 1966] for simple boundary conditions such as Mur [Mur, 1981] and Liao [Liao, 1984] conditions gives reflection of the order of 0.1 ... 1 %, but only if a wave is incident on the boundary at the right angle. When a wave is incident at an acute angle, the reflection coefficient increases to 100 % in case of tangential incidence. When using a continuous source, even such small reflections generated by the scheme in hand are, however, sufficient for accumulation of errors in the simulation area, hence the need for suppression methods such as PML (perfectly matched layer) used in FDTD models [Berenger, 1994]. It is this type of source that was applied in the experiments we present, which led to the need for the adaptation and use of the PML method. Splitting the scheme with respect to spatial variables and physical processes allows us to apply the profile of electric and magnetic losses, proposed by Berenger, directly to streams of the upstream scheme on the boundary of the simulation area. The geometric profile of losses within an individual layer has the form

$$\rho(r) = -\frac{\varepsilon_0 c_0 \ln(g)}{2\Delta x (g^N - 1)} \ln(R_0) g^{(r/\Delta x)}, \qquad (22)$$

where g is the geometric progression coefficient; Δx is the step in space; c_0 is the velocity of light; N is the PML number, counting from the interface of the computation area and boundary; r is the distance from the boundary; R_0 is the coefficient of reflection from the first layer. In the presented numerical experiments, we use the loss profile calculated from Formula (22) with the following parameters: R_0=0.01 (1 %), the progression coefficient g=2.15, the number of layers is 14. Despite the fact that the coefficient of reflection from the first layer is not less than that characteristic of the given scheme when zeroing outgoing streams at incidence angles of 80° to 90°, and in practice it is even larger due to reflections from subsequent layers, the main advantage of the PML method is its extremely weak dependence on the angle of electromagnetic wave arrival. This feature is also demonstrated by the version adapted for the upstream scheme.

RESULTS AND DISCUSSION

We have carried out numerical experiments of seven types: four experiments with the simulation area homogeneous in horizontal and vertical electron density profiles (Figure 1); three series of experiments with the transition in the direction of wave propagation (Figure 2). The simulated signal analyzed in all the numerical experiments was set by the sinusoidal function with a frequency of 1500 Hz. We do not discuss the transients associated with the beginning of the counting and the passage of the wave front through regions with non-zero horizontal gradient of electron density. All results discussed below have been obtained for the stable mode (the 30th–35th oscillation periods from the beginning of the simulation). It is therefore unreasonable to analyze directly temporal forms of electromagnetic signal components because they are identical to the original signal. Further, we compare and discuss some electromagnetic signal characteristics, such as amplitude and phase, as well as their derivatives.

Figure 3, *a* shows the percentage difference between amplitudes of the main wave electric field component for the cases of signal propagation when the entire region had an electron density profile characteristic of quiet conditions on March 16, 2013 at 06:00 UT and when the horizontal electron density profile had a transition from the quiet region to the region with increased electron density, which had a profile characteristic of the magnetic storm conditions on March 17, 2013 at 06:00 UT. Figure 3, *b* shows the difference between amplitudes of the main wave magnetic field component in the same experiments. Figure 4, *a*, *b* displays the amplitude difference of the main component of wave electric and magnetic fields for the cases of signal propagation when the entire region had an electron density profile typical of conditions of the magnetic storm on March 17, 2013 at 06:00 UT and when the horizontal electron density profile had a transition from the region with increased electron density to the quiet region, which had a profile characteristic of March 16, 2013 at 06:00 UT. We can see that propagation through the regions of both positive and negative horizontal electron density gradients has an effect on amplitude characteristics of electromagnetic waves, and the higher is the gradient in the transition region the stronger is the effect. However, in the case of weak electron density perturbations, changes in amplitudes of the main electromagnetic field components are not sufficient to be recorded by ground-based observation methods.

The analysis of electromagnetic wave propagation through the region with increased electron density located perpendicular to the propagation direction and parallel to the plane of the wave has revealed no significant effect on signal amplitude characteristics, irrespective of the ratio of bandwidth to wavelength. Obviously, a separate recording of electromagnetic field components cannot be used for analyzing weak perturbations of electron density in the ionosphere since the amplitude response to them does not exceed the background noise level.

The situation slightly improves in case of joint analysis of the electric and magnetic electromagnetic field components. Figure 5 plots the wave resistance of the medium, calculated as the ratio of the magnetic and electric fields for the cases of horizontally homogeneous medium with vertical profiles of all the types shown in Figure 1 and for the cases of propagation through the region with increased electron density λ and 0.25λ wide. Obviously, this approach can clearly distinguish the cases with the presence of regions with electron density perturbations in the ionosphere along a radio path from the cases of quiet conditions, but weakly reacts both to the magnitude of electron density perturbations and to the horizontal structure of these perturbations. To implement this approach, for the data analysis recorders in the case of a plane wave propagating in the plane of the Earth–ionosphere waveguide should detect the vertical electric field component and two horizontal magnetic field components.

In the case of waves of another type or arbitrary propagation direction, it is necessary to fix all the six electromagnetic field components.

Figure 6 shows phase differences between magnetic and electric field strengths for the cases of horizontally homogeneous medium with vertical profiles of all types, shown in Figure 1, and for the cases of propagation through the region with increased electron density λ and 0.25λ wide. We can see that the phase characteristics are most clearly differentiated depending on the intensity of

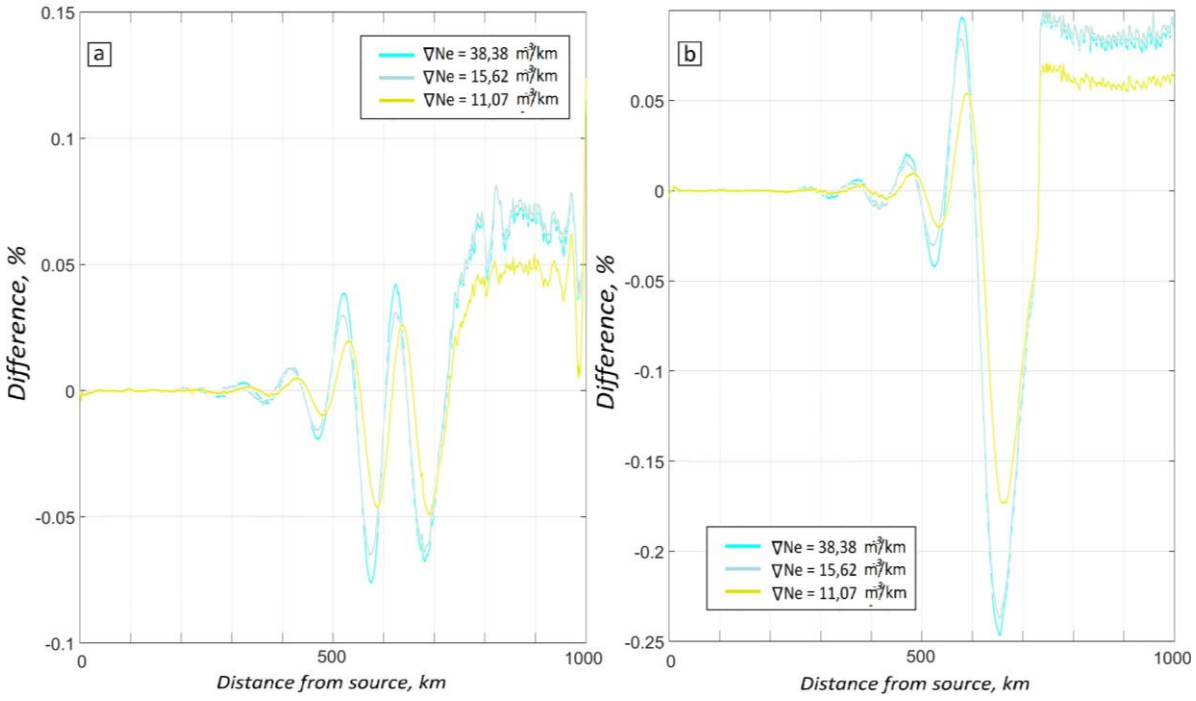

Figure 3. Percentage difference between amplitudes for electric (*a*) and magnetic (*b*) fields for signal propagation when the entire region had an electron density profile characteristic of the quiet conditions on March 16, 2013 at 06:00 UT and when the horizontal electron density profile had a transition from the quiet region to the region with increased electron density

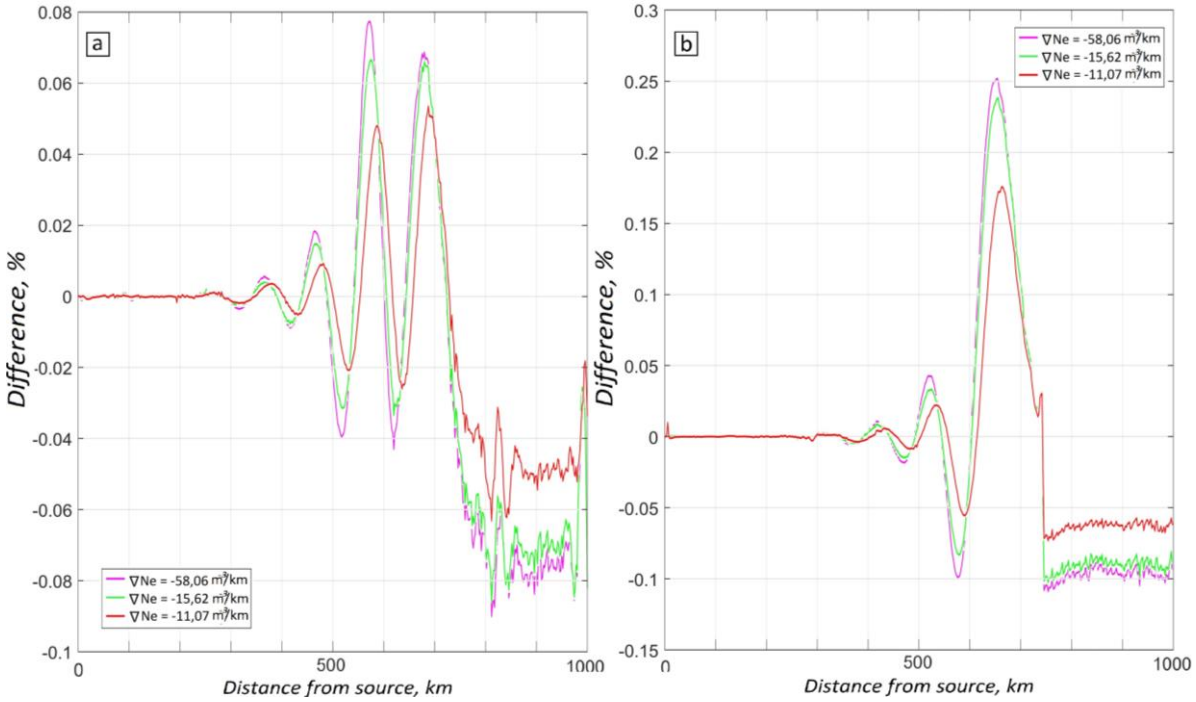

Figure 4. Percentage difference between amplitudes for signal propagation cases when the entire region had an electron density profile of the magnetic storm conditions on March 17, 2013 at 06:00 UT and when the horizontal electron density profile had a transition from a region with increased electron density to a quiet region: electric field strength (*a*); magnetic field strength (*b*)

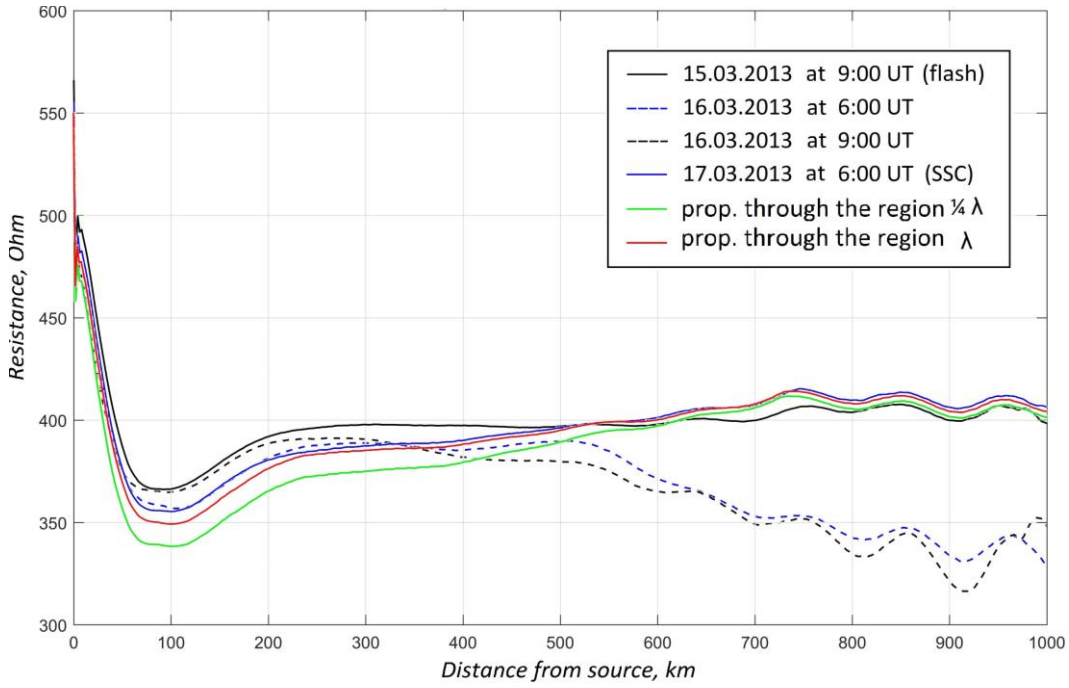

Figure 5. Wave resistance of the medium

of electron density perturbation both for changing vertical electron density profile and for the horizontal profile as compared with the previously considered ones. The question remains as to perturbation of what type caused the phase change in each case.

The question also remains about the dependence of the phase shift on the form of the electron density profile as well as its value for waves of different ranges. These and many other questions require further study, which is beyond the scope of this paper.

To analyze phase characteristics, it is necessary when recording electromagnetic field components to make an accurate time reference of the recorded electric and magnetic components. In case of development of a network of receivers, which can help to identify horizontal ionospheric irregularities, it is necessary to provide an accurate time reference of the recorded field components to the universal time, as in [Pilgaev et al., 2008].

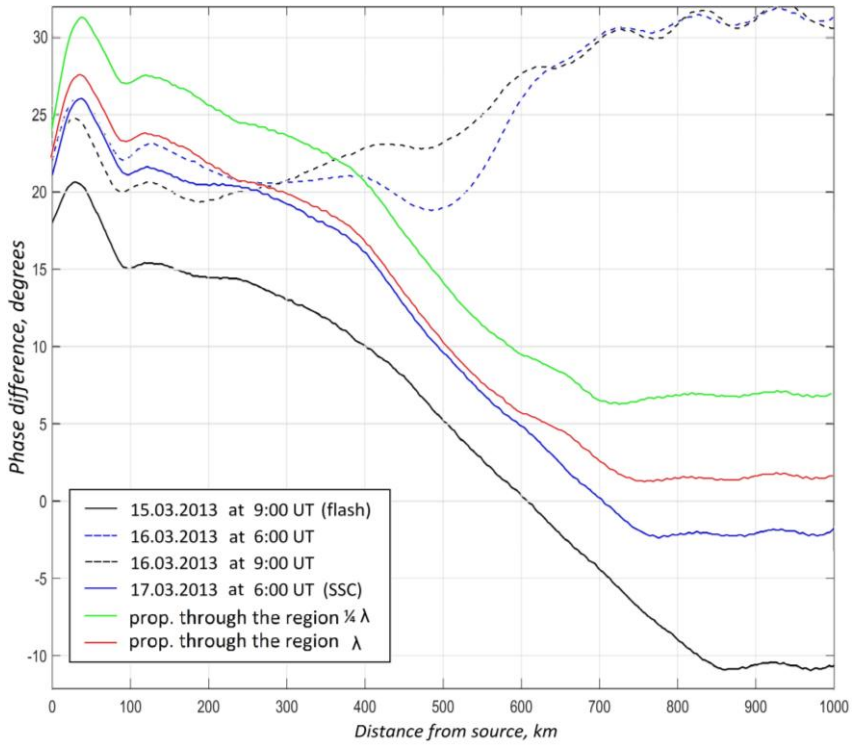

Figure 6. Phase difference between electric and magnetic field strengths

CONCLUSION

We have used numerical experiment methods to determine characteristics of ELF electromagnetic waves recorded in the surface layer, which provide the maximum amount of information about the state of the Earth–ionosphere waveguide.

We have found an effect of horizontal gradients of electron density on the amplitude of ELF electromagnetic signals at the transition between regions with different characteristics of the Earth–ionosphere waveguide. We have shown that in case of minor electron density changes electromagnetic signal amplitude changes are negligible and do not exceed 1 %.

We have revealed that the vertical electron density profile has a significant effect on the wave resistance of the medium and on the phase difference between magnetic and electric components. We have shown that if electron density increases in the D-region the wave resistance of the medium increases too, and the electromagnetic field component *E* begins to lag behind *H*. We think that the phase lag of the electric field behind the magnetic field is due to inertia of electrons and their collisions with neutral particles of the ionosphere. The electric current density induced by the electric field of the signal affects the phase shift between the moments when electric and magnetic fields of the signal reach maximum values at a fixed point of the ionosphere.

The calculations lead to the conclusion that the ground-based systems of ELF wave detection the least suitable for monitoring the state of the ionosphere should contain three recorders: one for the vertical electric component and two for the horizontal magnetic component of the electromagnetic field. For this purpose, it is important to provide proper synchronization between the recorders and the universal time.

The research was supported by RSF (project No. 18-77-10018).

REFERENCES

Akimov V.F., Kalinin Yu.K. *Vvedenie v proektirovanie ionosfernykh zagorizontnykh radiolokatorov* [Introduction to the Design of Ionospheric Over-the-Horizon Radars]. Moscow, Tekhnosfera Publ., 2017, 492 p. (In Russian).

Berenger J.-P. A perfectly matched layer for the absorption of electromagnetic waves. *J. Computational Phys.* 1994, vol. 114, no. 2, pp. 185–200. DOI: 10.1006/jcph.1994.1159.

Bisikalo D.V., Zhilkin A.G., Boyarchuk A.A. Gazodinamika tesnykh dvoinykh zvezd [Gas Dynamics of Close Binary Stars]. Moscow, Fizmatlit Publ. 2013, 632 p. (In Russian).

Korja T., Engels M., Zhamaletdinov A.A., Kovtun A.A., Palshin N.A., Maxim Yu, et al. Crustal conductivity in Fennoscandia — a compilation of a database on crustal conduc ance in the Fennoscandian shield. *Earth, Planets and Spac*. 2002, vol. 54, no. 5, pp. 535–558. DOI: 10.1186/BF03353044.

Kovenja V.M., Janenko N.N. *Metod rasshchepleniya v zadachakh gazovoi dinamiki* [Splitting method in problems of gas dynamics]. Novosibirsk, Nauka Publ., 1981, 304 p. (In Russian).

Kulikovskij A.G., Pogorelov N.V., Semenov A.Ju. Matematicheskie voprosy chislennogo resheniya giperbolicheskikh sistem uravnenii [Mathematical questions in numerical solution of hyperbolic combined equations]. Moscow, Fizmatlit Publ. 2012, 656 p. (In Russian).

Liao Z.P., Wong H.L., Yang B.P., Yuan Y.F. A transmitting boundary for transient wave analyses. *Scienta Sinica. Ser. A.* 1984, vol. 27, no. 10, pp.1063–1076.

Mingalev I.V., Mingalev O.V., Akhmetov O.I., Suvorova Z.V. The apparent splitting scheme for Maxwell's equations. *Matematicheskoe modelirovanie* [Mathematical

Models and Computer Simulations]. Moscow, RAN Publ., 2018a, vol. 30, no. 12, pp. 17–38. (In Russian). DOI: 10.31857/S0234087 90001934-1.

Mingalev O.V., Mingalev I.V., Melnik M.N., Akhmetov O.I., Ахметов О.И., Suvorova Z.V. New method of the Vlasov–Maxwell system numerical integration. *Matematicheskoe modelirovanie* [Mathematical Models and Computer Simulations]. Moscow, RAN Publ. 2018b, vol. 30, no. 10, pp. 21–43. (In Russian). DOI: 10.31857/S023408790001919-4.

Mur G. Absorbing boundary conditions for the finite-difference approximation of the time domain electromagnetic field equations. *IEEE Electromagnetic Compatibility*, 1981, vol. 23, no. 4, pp. 277–382. DOI: 10.1109/TEMC.1981.303970.

Pilgaev S.V., Akhmetov O.I., Filatov M.V., Fedorenko Ju.V. The universal device of data synchronization by the GPS receiver. *Pribory i tekhnika eksperimenta [Instruments and Experimental Techniques]*. Moscow, RAN Publ. 2008, no. 3, pp. 175–176. (In Russian).

Tereshhenko VD, Vasilyev EB, Ovchinnikov NA, Popov AA The middle wave radar of Polar geophysical institute for the lower ionosphere research. *Tehnika i metodika geofizicheskogo jeksperimenta* [Technology and Methods of Geophysical Experiment], Apatity, Kola Science Center RAS, 2003, pp. 37–46. (In Russian).

Voskresenskii D.I., Stepanenko V.I., Filippov V.S. *Ustroi stva SVCh i antenny. Proektirovanie fazirovannykh antennykh reshetok* [Microwave oven devices and antennas. Designing of the phased antenna lattices]. Moscow, Radiotehnika Publ. 2012, 744 p. (In Russian).

Yee Kane. Numerical solution of initial boundary value problems involving Maxwell's equations in isotropic media. *IEEE Transactions on Antennas and Propagation*, 1966, vol. 14, pp. 302–307. DOI: 10.1109/TAP.1966.1138693.

How to cite this article

Akhmetov O.I., Mingalev I.V., Mingalev O.V., Suvorov Z.V., Belakhovsky V.B., Chernyakov S.M. Determination of ELF wave characteristics most strongly reacting to minor changes of ionospheric electron density in a high-latitude region. *Solar-Terrestrial Physics*. 2019. Vol. 5. Iss. 4. P. 81–90. DOI: 10.12737/stp-54201911.